Journal of Solid State Chemistry **158,** 279–289 (2001)
doi:10.1006/jssc.2001.9108, available online at http://www.idealibrary.com on IDEAL®

Synthesis, Structure, and Electrical Conductivity of $A'[A_2B_3O_{10}]$ ($A' = Rb, Cs; A = Sr, Ba; B = Nb, Ta$): New Members of Dion–Jacobson-Type Layered Perovskites

Venkataraman Thangadurai,* Peter Schmid-Beurmann,† and Werner Weppner*

*Chair for Sensors and Solid State Ionics, Faculty of Engineering, Christian Albrechts University of Kiel, Kaiserstr. 2, 24143 Kiel, Germany; and †Institute for Geosciences, Christian Albrechts University of Kiel, Ohlshausenstr. 40, 24098 Kiel, Germany
E-mail: vt or ww@tf.uni-kiel.de, psb@min.uni-kiel.de

Received October 17, 2000; in revised form January 3, 2001; accepted January 19, 2001

New members of Dion–Jacobson (D-J)-type layered perovskites of the general formula $A'[A_2B_3O_{10}]$ (A' = Rb, Cs; A = Sr, Ba; B = Nb, Ta) were prepared by solid-state reactions between the metal oxides, nitrates, and carbonates under specific conditions. The crystal structures were determined using powder X-ray diffraction data in combination with Rietveld analysis. The *c*-axis lattice parameter increases as the size of the alkaline earth ion increases. Both Sr and Ba compounds crystallize in a tetragonal cell, while the corresponding Ca compounds crystallize in an orthorhombic cell. The electrical conductivity of the layered perovskites was determined using AC impedance analysis and DC methods. Among the compounds with the same alkali ion and different alkaline earth ions, the Ca compound exhibits a higher electrical conductivity than the corresponding Sr and Ba compounds. DC measurements reveal that the layered perovskites exhibit both ionic and electronic conduction.

Key Words: **D–J type layered perovskites; Rietveld refinement; electrical conductivity; ac impedance; layered niobates; perovskites.**

1. INTRODUCTION

Layered (2D) perovskites derived from the three-dimensional (3D) ABO_3 perovskites are two types with the general formula $A'[A_{n-1}B_nO_{3n+1}]$ and $A'_2[A_{n-1}B_nO_{3n+1}]$, where A' is a monovalent ion, A is a divalent alkaline earth metal ion and B is a tetravalent or pentavalent transition metal ion. The first series of oxides is known as Dion–Jacobson (D-J) (1)-type and the latter series of oxides is known as Ruddlesden–Popper (R-P) (2)-type layered perovskites. The thickness of the perovskite slab is given by the value n that determines the number of BO_6 octahedra corner shared along the c axis. $KCa_2Nb_3O_{10}$ (1) and $K_2La_2Ti_3O_{10}$ (3) are typical examples for $n = 3$ members of the D-J and R-P layered perovskites, respectively. Both types of layered perovskites are a unique class of materials exhibiting novel physical properties and interesting chemical reactivity (1, 4). For example, alkali ions in these layered perovskites undergo ion exchange with molten salts or under acidic conditions. The layered perovskites are especially potentially important materials because of their various technology-related properties such as ionic conductivity (5), dielectricity (6), superconductivity (7), luminescence (8), photocatalytic activity (9), magnetism (10), and giant magnetoresistivity (11).

The difference between the D-J and R-P series of layered perovskites lies in the interlayer alkali ion density. The D-J series of layered perovskites has a lower density that favors ion exchange and higher ionic conductivity as compared to the R-P series (12). Several members of both types of layered perovskites are reported in the literature (1, 4, 13). Solid solutions of compounds of the D-J and R-P series with variable interlayer alkali ion densities were also investigated (13). To our knowledge, the replacement of Ca in the D-J series by other divalent alkaline earth ions is not reported so far in the literature, in contrast to studies of the R-P series. For example, trivalent La in $Li_2La_2Ti_3O_{10}$ has been substituted by divalent Ca and Sr which yields new cation deficient R-P phases (14), $Li_2A_{1.5}Nb_3O_{10}$ (A = Ca, Sr), with similar ion exchange properties under acidic conditions (14). Also, the tetravalent Ti ion has been substituted by pentavalent Nb and Ta. Very recently layered perovskites of the series $CsA_2Nb_3O_{10}$ (A = Ca, Sr, Ba) have been investigated using Raman spectra (15). In view of the interesting physical properties and chemical reactivity of the D-J series, we have investigated the replacement of Ca by other alkaline earth ions and studied their structural and electrical conductivity properties.

2. EXPERIMENTAL PROCEDURES

2.1. Synthesis

Materials with the composition $A'[A_2B_3O_{10}]$ (A' = Rb, Cs; A = Sr, B = Nb, Ta) were prepared by conventional

0022-4596/01 $35.00

TABLE 1
Chemical Composition and Synthesis Conditions of $A'[A_2B_3O_{10}]$ (A' = K, Rb, Cs; A = Ca, Sr, Ba; B = Nb, Ta)

Composition	Temp.[a] (°C)/time (h)
$RbSr_2Nb_3O_{10}$	650/12, 900/3, 1150/1
$CsSr_2Nb_3O_{10}$	900/6, 1250/24, 1300/12
$CsBa_2Nb_3O_{10}$	600/6, 850/3
$CsSr_2Ta_3O_{10}$	900/12, 1150/12
$KSr_2Nb_3O_{10}$	900/6, 1250/(24 + 12)

[a] Powders were ball-milled for about 3 h after each heat treatment.

solid-state reaction of appropriate mixtures of high purity $A'NO_3$, ACO_3, $A(NO_3)_2$, and B_2O_5 (> 99.0% purity, obtained from Fluka/Aldrich) at elevated temperatures. An excess of 30 wt% of alkali nitrate was used to compensate the loss of the alkali component due to evaporation. Any alkali excess was washed out after the reaction with distilled water and the samples were dried at room temperature. The chemical compositions and synthesis conditions of all samples are given in Table 1. $CsCa_2Nb_3O_{10}$ was prepared by reacting $CsNO_3$, $CaCO_3$, and Nb_2O_5 as described in Ref. 1.

We could readily synthesize only one Ba-containing compound, $CsBa_2Nb_3O_{10}$, among the series $A'[Ba_2B_3O_{10}]$ under mild conditions since the reaction product between the nitrates and oxides melt at synthesis conditions similar to those of the Sr compounds. Several attempts were made using different synthesis conditions by varying the alkali content and the sintering temperatures. For instance, using 100 wt% excess of alkali metal nitrates, we did not see any indication for the formation of the layered compound in the temperature range 600–1000°C. Thermal Gravimetric Analysis (TGA) and Differential Thermal Analysis (DTA) investigations were performed using a NETZSCH Thermal Analysis device (Model STA-409) to understand the decomposition/reaction steps of appropriate mixtures of the reactants containing 30 wt% excess of alkali nitrates in flowing argon gas. We see a single-step (Fig. 1) weight loss for all compositions with A = Ba between 500 and 750°C with a "knee" above 600°C according to the assumed chemical/ decomposition reaction:

$$1.3A'NO_3 + 2Ba(NO_3)_2 + 1.5Nb_2O_5 \rightarrow$$

$$A'[Ba_2Nb_3O_{10}] + 5.3NO_2 + 0.15A'_2O + 1.325O_2$$

The expected weight losses for the decomposition reaction mixtures for the formation of layered compounds with the compositions $RbBa_2Nb_3O_{10}$ and $CsBa_2Nb_3O_{10}$ are 28.23 and 27.96 wt%, respectively. We observed about 26 wt% weight loss according to the TGA curves (Fig. 1), suggesting that the decomposition reactions are completed at around 800°C. Thus, one would expect the formation of the layered compounds by annealing at around 800°C.

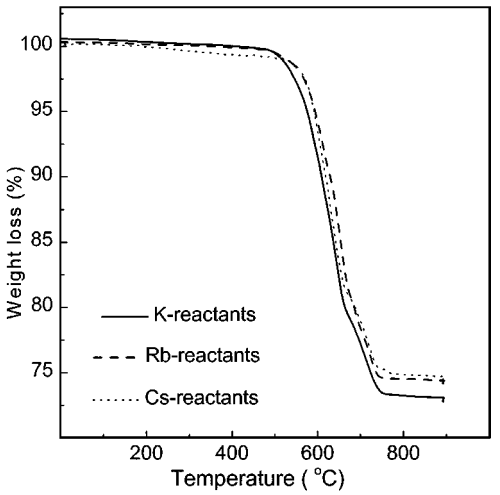

FIG. 1. TGA curves obtained for the chemical/decomposition reaction: $1.3A'NO_3 + 2Ba(NO_3)_2 + 1.5Nb_2O_5 \rightarrow A'Ba_2Nb_3O_{10} + 5.3NO_2 + 0.15A'_2O + 1.325\ O_2$. ($A'$ = K, Rb, Cs).

Accordingly, the synthesis reactions were performed at 850°C for the Ba compounds. After the reaction, the products were washed and dried in air at room temperature and the phase formations were examined.

2.2. X-Ray Powder Diffraction

Phase analysis of the products was carried out by X-ray powder diffraction (XRD) using a SIEMENS D-5000 powder diffractometer with Cu$K\alpha$ radiation and a secondary graphite (001) monochromator with the operation conditions V = 40 kV and I = 30 mA. The impurity phases present in the samples were identified using the standards from the JCPD-ICCD database with the help of the Siemens DIFFRAC-AT software package. Quantitative phase analysis was performed using the Rietveld programs HILL8 (16) and FULLPROF (17). The samples were ground in an agate mortar and 30–40 mg of the powder was dispersed using a sieve (120 mesh) onto glass sample holders covered by a thin film of vaseline in order to reduce the texture effect. The weight portions of the impurity phases present in the products were determined using multiphase Rietveld refinement of the XRD data. Diffraction data from 17 to 100° (2θ) were included into the calculation.

2.3. Electrical Conductivity

Electrical conductivity measurements were carried out employing sintered bodies in air. Single-phase perovskite powders were isostatically pressed into cylindrical pellets under a pressure of 38 kN/cm^2. The pellets were annealed in air for 24 h at the same temperature at which the polycrystalline samples were prepared, except for $CsBa_2Nb_3O_{10}$, which was sintered for only 3 h. To avoid any alkali loss

during the sintering, the pellets were covered with the powder of the sample material. After sintering, the cylindrical pellet was cut into small coin-shaped pellets (10 mm in diameter and about 2–3 mm in thickness) using a diamond saw. The flat pellet surfaces were coated with Pt paste and cured at 800°C for 1 h. Impedance data were obtained in the frequency range from 100 Hz to 13 MHz at 100–850°C, employing an HP 4192 A impedance analyzer. In order to achieve equilibrium conditions, the samples were equilibrated at constant temperature for about 3 h prior to each measurement. DC electrical conductivity measurements were also made in air at 620°C for $RbSr_2Nb_3O_{10}$.

3. RESULTS AND DISCUSSION

3.1. Phase Analysis

The synthesis experiments resulted in white fine-grained powders. The optical inspection using a transmission light microscope revealed that the compounds were present in the shape of irregular crystals with sizes less than 10 μm except for a few crystals reaching diameters of 30 μm. The powder X-ray diffraction patterns of the compounds $RbSr_2Nb_3O_{10}$, $CsSr_2Nb_3O_{10}$, $CsBa_2Nb_3O_{10}$, and $CsSr_2Ta_3O_{10}$ showed the typical formation of the $n = 3$ member of D-J layered compounds (1, 18–20). In contrast to that we were not able to obtain single-phase layered perovskite D-J type Ba-compounds containing K and Rb under our synthesis conditions. The TGA decomposition reaction products of both K and Rb reactants do not show the formation of the D-J-type layered perovskites (Fig. 2). Instead, an impurity phase, $Ba_4Nb_5O_{15}$, is seen in the powder XRD patterns (Figs. 2a and 2b). In contrast, in the TGA products of the Cs compound, the $n = 3$ D-J-type layered perovskite was found as the main phase with only a small amount of $Ba_4Nb_5O_{15}$ (Fig. 2c). The TGA experiments of all single-phase perovskites show that no weight loss occurs up to 850°C, suggesting that the compounds are thermally stable and anhydrous.

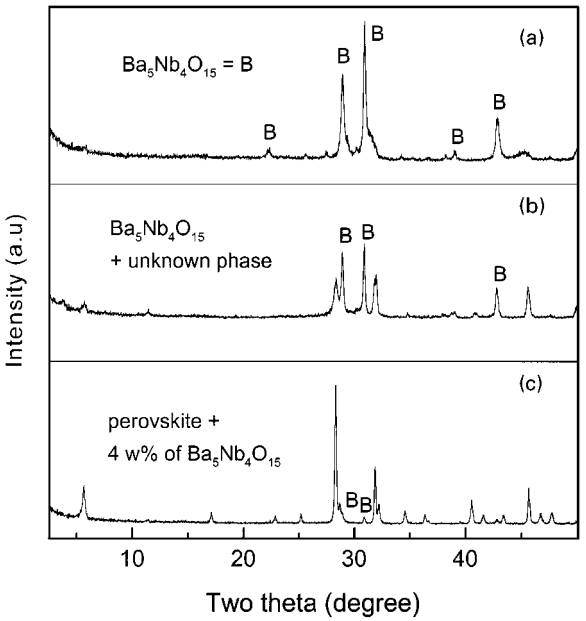

FIG. 2. Powder XRD patterns (Cu$K\alpha$) of the TGA reaction products assuming the formation of the layered compounds (a) $KBa_2Nb_3O_{10}$, (b) $RbBa_2Nb_3O_{10}$, and (c) $CsBa_2Nb_3O_{10}$. Impurity phase, due to $Ba_5Nb_4O_{15}$ is marked by "B".

3.2. Structure Refinement

Powder XRD of the new layered perovskites $RbSr_2Nb_3O_{10}$, $CsSr_2Nb_3O_{10}$, $CsBa_2Nb_3O_{10}$, and $CsSr_2Ta_3O_{10}$ could be indexed by a tetragonal symmetry. No reflection conditions were found, thus suggesting the eight possible space groups of *P*4, $P\bar{4}$, *P*4/*m*, *P*422, *P*4*mm*, $P\bar{4}m2$, $P\bar{4}2m$, and *P*4/*mmm*. These results correspond to that of the compound $CsCa_2Ta_3O_{10}$ (18). Therefore, the structural data of $CsCa_2Ta_3O_{10}$ were used as starting parameters for the Rietveld refinement. The final atomic positions are given in Table 2 and the final profile fits for $RbSr_2Nb_3O_{10}$, $CsSr_2Nb_3O_{10}$, $CsBa_2Nb_3O_{10}$, and $CsSr_2Ta_3O_{10}$ are given in Figs. 3 and 4. Satisfying fits were obtained for the perovskites with reasonable *R* values (Table 2). The idealized structures of the representative perovskites are shown together with $CsCa_2Nb_3O_{10}$ in Fig. 5 (20).

It should be mentioned that in our attempts to prepare the corresponding K compounds, we could prepare the nearly single-phase Sr compound $KSr_2Nb_3O_{10}$ which can be indexed by an orthorhombic unit cell with lattice constants $a = 3.913(1)$, $b = 29.960(5)$, and $c = 3.902(1)$ Å. As the material is very sensitive to a texture effect it cannot be excluded that the remaining differences between the observed and the calculated intensities are due to preferred orientation. Single-crystal growth of $KSr_2Nb_3O_{10}$ will be essential to determine the correct structure.

3.3. Structure Description

The main difference between the structures of the alkali metal layered niobate perovskites is that of triple-perovskite layer stacking as observed in the related perovskites with the general formula $ACa_2B_3O_{10}$. The characteristic sequence of adjacent perovskite layer ($(Ca_2B_3O_{10})^-$) stacking is given by a distinct shift vector (defined as *sh*) of perovskite layers in the direction perpendicular to the *c*- or *a*-axis that depends on the setting of the appropriate space group. This shift depends on the nature/size of the alkali metal cations (1, 19, 20). For example, in the case of the large alkali metals like Rb and Cs, alternating perovskite slabs are stacked together without any shift: $sh = (0, 0, 0)$ (1, 19). In contrast to

TABLE 2
Final Atomic Positions and Thermal Parameters of $A'[A_2B_3O_{10}]$ (A' = Rb, Cs; A = Ca, Sr, Ba; B = Nb, Ta)

		Atom	Site	x	y	Z	B	SOF
$RbSr_2Nb_3O_{10}$		Rb	1*d*	0.5	0.5	0.5	3.4(3)	1
P4/mmm (No. 123)		Sr	2*h*	0.5	0.5	0.1461(4)	2.0(1)	1
$a = 3.8944(2)$ Å		Nb(1)	1*a*	0	0	0	1.6(1)	1
$c = 15.2710(8)$ Å		Nb(2)	2*g*	0	0	0.2887(3)	1.6(1)	1
$R_{wp} = 9.5\%$	$R_p = 7.6\%$	O(1)	2*f*	0	0.5	0	2.3(4)	1
$R_I = 4.1\%$	$R_F = 2.2$	O(2)	2*g*	0	0	0.129(2)	2.3(4)	1
$w = 0.0243(4)$	$n_a = 0.84(1)$	O(3)	4*I*	0	0.5	0.265(2)	2.3(4)	1
Asy = −0.016(7)		O(4)	2*g*	0	0	0.400(2)	2.3(4)	1
$CsSr_2Nb_3O_{10}$		Cs	1*d*	0.5	0.5	0.5	3.1(4)	1
P4/mmm (No. 123)		Sr	2*h*	0.5	0.5	0.1445(8)	1.5(3)	1
$a = 3.9077(5)$ Å		Nb(1)	1*a*	0	0	0	1.1(2)	1
$c = 15.414(2)$ Å		Nb(2)	2*g*	0	0	0.2839(6)	1.1(2)	1
$R_{wp} = 9.8\%$	$R_p = 8.0\%$	O(1)	2*f*	0	0.5	0	1.5(7)	1
$R_I = 3.8\%$	$R_F = 1.81$	O(2)	2*g*	0	0	0.128(3)	1.5(1)	1
$w = 0.042(1)$	$n_a = 1.05(2)$	O(3)	4*i*	0	0.5	0.258(3)	1.5(1)	1
Asy = 0.001(5)		O(4)	2*g*	0	0	0.390(4)	1.5(1)	1
$CsBa_2Nb_3O_{10}$		Cs	1*d*	0.5	0.5	0.5	2.2(2)	1
P4/mmm (No. 123)		Ba	2*h*	0.5	0.5	0.1437(2)	1.4(1)	1
$a = 3.9766(1)$ Å		Nb(1)	1*a*	0	0	0	1.0(1)	1
$c = 15.5792(7)$ Å		Nb(2)	2*g*	0	0	0.2908(3)	1.0(1)	1
$R_{wp} = 10.6\%$	$R_p = 8.3\%$	O(1)	2*f*	0	0.5	0	0.6(3)	1
$R_I = 3.6\%$	$R_F = 2.2$	O(2)	2*g*	0	0	0.122(2)	0.6(3)	1
$w = 0.0239(4)$	$n_a = 0.61(1)$	O(3)	4*i*	0	0.5	0.268(1)	0.6(3)	1
Asy = −0.03(1)		O(4)	2*g*	0	0	0.402(2)	0.6(3)	1
$CsSr_2Ta_3O_{10}$		Cs	1*d*	0.5	0.5	0.5	1.8(1)	1
P4/mmm (No. 123)		Sr	2*h*	0.5	0.5	0.1442(4)	0.9(1)	1
$a = 3.8990(1)$ Å		Ta(1)	1*a*	0	0	0	0.69(5)	1
$c = 15.5359(3)$ Å		Ta(2)	2*g*	0	0	0.2832(2)	0.69(5)	1
$R_{wp} = 7.5\%$	$R_p = 5.9\%$	O(1)	2*f*	0	0.5	0	1.5(3)	1
$R_I = 2.7\%$	$R_F = 1.55$	O(2)	2*g*	0	0	0.128(2)	1.5(3)	1
$w = 0.0191(2)$	$n_a = 0.53(1)$	O(3)	4*i*	0	0.5	0.257(1)	1.5(3)	1
Asy = −0.01(1)		O(4)	2*g*	0	0	0.396(2)	1.5(3)	1

that, in the case of K as alkali metal, alternating perovskite slabs are shifted by one half of a basal lattice parameter: $sh = (\frac{1}{2}, 0, 0)$. In the case of Na and Li compounds, the shift occurs parallel to the diagonal of the basis plane: $sh = (\frac{1}{2}, \frac{1}{2}, 0)$ (19). The same sequence of layer stacking can be observed in the new investigated layered perovskites with the formula $A'A_2Nb_3O_{10}$ (A' = Rb, Cs; A = Sr, Ba) of the present work. Therefore, these observations characterize a general trend in the crystal chemical properties of these perovskite phases.

The effect of the different alkali and alkaline earth ions on the *c*-lattice parameter of the crystallographic axis perpendicular to the layer plane, which is defined by the perovskite slabs or the alkali layers of the layered perovskites, is plotted in Fig. 6. For the purpose of comparison, the lattice parameters are presented together with those of the Ca-compounds and are plotted in the form of *a*, *c*, or 2*c*. In each series, $A'A_2Nb_3O_{10}$ (19), this lattice parameter is increasing with increasing atomic number of the alkali metal. This behavior can be easily explained by the increasing size of alkali ion and alkali–oxygen bond lengths in $A'Ca_2Nb_3O_{10}$ (1).

A'^+	Na-α	Na-β	K	Rb	Cs
d(Å)	2.54	2.34	2.78	2.96	3.16

For a given alkali ion, the *c*-lattice parameter is further increased when going from Ca to Ba. This can be seen clearly from comparing the lattice parameters of $CsCa_2Nb_3O_{10}$ ($a = 30.185$ Å) (20), $CsSr_2Nb_3O_{10}$ ($2c = 30.828$ Å) and $CsBa_2Nb_3O_{10}$ ($2c = 31.1584$ Å). The simple explanation is given by the larger Sr^{2+}(1.44 Å) and

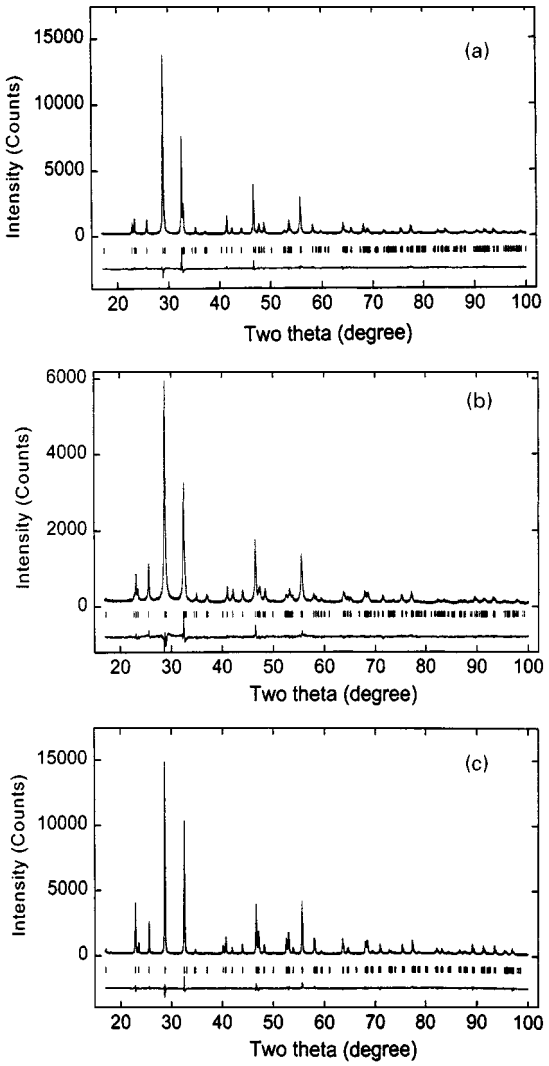

FIG. 3. Observed (line), calculated (points), and difference XRD patterns (Cu$K\alpha$) of (a) $RbSr_2Nb_3O_{10}$, (b) $CsSr_2Nb_3O_{10}$, and (c) $CsSr_2Ta_3O_{10}$.

Ba^{2+}(1.60 Å) ions, which substitute the smaller Ca^{2+} (1.35 Å) ions (21). Parallel to the general increase of the *c*-lattice parameter, the thickness of the alkali interlayer space (distance between the adjacent perovskite slab) has a maximum for the Sr compound (Fig. 7b), whereas the thickness of the perovskite slab remains constant when going from Ca to Sr, and increases when Sr^{2+} is substituted against Ba^{2+} ions (Fig. 7). Selected bond lengths are listed in Table 3. The interlayer alkali metal ion in both Sr- and Ba-containing compounds are distinctly different from that of the corresponding Ca compounds. In the Ca compound, there are two types of Cs ions (20). The Cs–O bond distances are in the range 3.02–3.29 Å (20), while the Sr and Ba compounds have only one type of Cs ion with the bond distances of 3.24 and 3.20 Å, respectively (Table 3).

3.4. Electrical Properties

3.4.1. AC impedance. Typical impedance plots obtained in air for the layered perovskites at 550 and 700°C are shown in Figs. 8 and 9, respectively. We see semicircles for most of the layered perovskites including $CsBa_2Nb_3O_{10}$ with 4 wt% of $Ba_5Nb_4O_{15}$ as a second phase, which is considered to be too small to have an influence on the electrical properties. $RbSr_2Nb_3O_{10}$ shows two semicircles corresponding to bulk and grain-boundary contributions to the conductivity which are of the same order of magnitude. However, we did not clearly see both grain-boundary and bulk contributions over the entire temperature range of the measurements (Fig. 9). Thus, we have taken uniformly the total resistance from the low-frequency minimum along the Z'-axis of the impedance plots. Hence, the conductivity data reported for $RbSr_2Nb_3O_{10}$ combine both bulk and grain boundary contributions.

Arrhenius plots of the electrical conductivity are shown in Figs. 10–12. Since the materials are anhydrous, the possibility of proton conduction is excluded. We believe that the observed conductivity is due to the migration of alkali ions in between the perovskite slabs besides electronic charge carriers. Table 4 gives a summary of the electrical conductivity data of the various investigated layered perovskites. For the purpose of comparison, we also measured the electrical conductivity of the Ca compound, $CsCa_2Nb_3O_{10}$, and these data are also shown in Fig. 11. The electrical conductivity values of the $CsCa_2Nb_3O_{10}$ compound are similar to those reported in the literature (1). We see that the conductivity values obtained upon the first heating and cooling cycle fall on the same line, indicating the true conductivity of the sample. Among the layered perovskites, $KSr_2Nb_3O_{10}$ exhibits the highest electrical conductivity of 1.46×10^{-4} S/cm at 700°C with the lowest activation energy of 0.70 eV (Table 4). It is also observed that compounds containing the same alkaline earth ion, the K-compounds exhibit the highest conductivity compared to the Rb and Cs compounds. This is clearly seen by comparing the conductivity data of $KSr_2Nb_3O_{10}$, $RbSr_2Nb_3O_{10}$ and $CsSr_2Nb_3O_{10}$ at 700°C (Table 4). Among the compounds with the same alkali ion and different alkaline earth ions, the Ca compound exhibits the highest conductivity of 1.45×10^{-5} S/cm at 700°C, while the corresponding Sr and Ba compounds exhibit conductivities of 6.01×10^{-6} and 3.45×10^{-6} S/cm, respectively, at the same temperature. This is clearly seen by comparing the conductivity values of $CsCa_2Nb_3O_{10}$, $CsSr_2Nb_3O_{10}$, and $CsBa_2Nb_3O_{10}$ (Table 4).

Among the series $CsA_2Nb_3O_{10}$ (A = Ca, Sr, Ba), the highest electrical conductivity of $CsCa_2Nb_3O_{10}$ suggests that the optimum thickness of the interlayer (in between the two triple-layered perovskite slabs) for the Cs–ion conduction is around 3.16 Å (Fig. 7). Furthermore, longer Cs–O bonds (Table 3) and the tilting of the NbO_6 octahedra

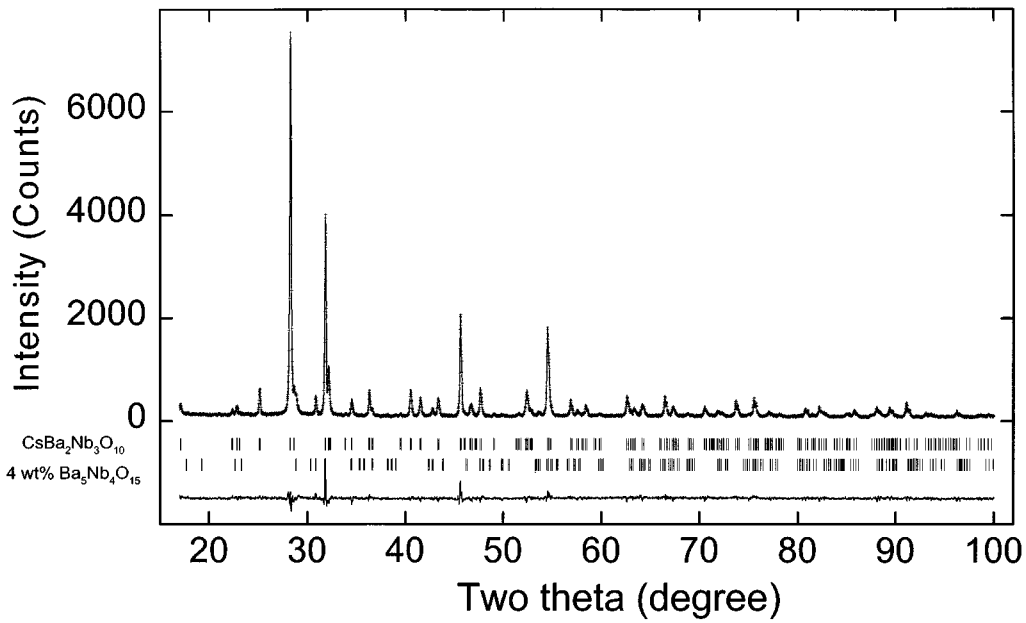

FIG. 4. Observed (line), calculated (points), and difference XRD patterns (Cu$K\alpha$) of $CsBa_2Nb_3O_{10}$.

favors the conductivity in Ca compounds compared to Sr and Ba compounds (Fig. 5). In addition, assuming ionic transport, the high conductivity can be explained using free energy considerations of the alkaline oxide formations. The Gibbs free energy at 300 K of the alkaline oxide formation follows the order CaO (551.6 kJ/mol) > SrO (511.2 kJ/mol) > BaO (477.7 kJ/mol) (22). The Ca–O bond is much stronger than that of Sr–O and Ba–O bonds. Thus, alkali ions (A') bound to oxygen with the competion of Ca–O bonds are expected to be weakly bound to the anions

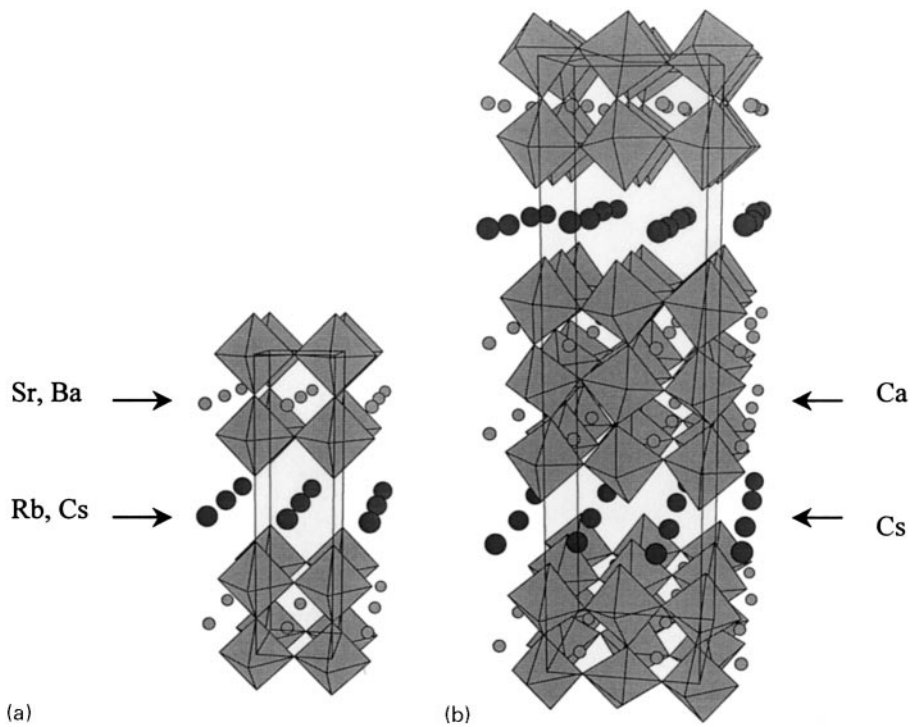

FIG. 5. Idealized structures of (a) $A'A_2B_3O_{10}$ (A' = Rb, Cs; A = Sr, Ba; B = Nb, Ta) and (b) $CsCa_2Nb_3O_{10}$ (20).

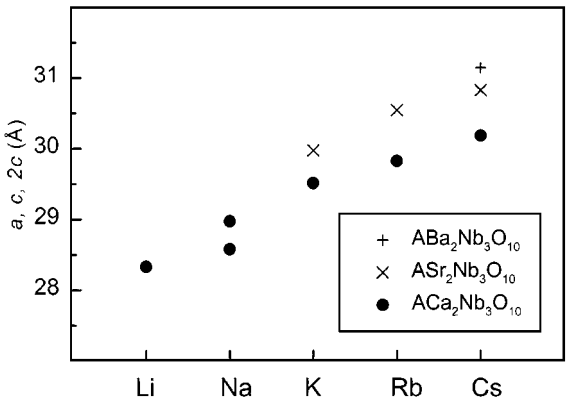

FIG. 6. Lattice parameters (a, c, or $2c$) perpendicular to the plane defined by the perovskite slab or the alkali layer of various layered perovskites with the general formula of $A'A_2Nb_3O_{10}$. For better comparison the lattice parameter: a for $KSr_2Nb_3O_{10}$; c for Li-, Na-, K-, and Cs- in the series $ACa_2Nb_3O_{10}$; and $2c$ for $RbCa_2Nb_3O_{10}$, $RbSr_2Nb_3O_{10}$, $CsSr_2Nb_3O_{10}$, and $CsBa_2Nb_3O_{10}$ are shown.

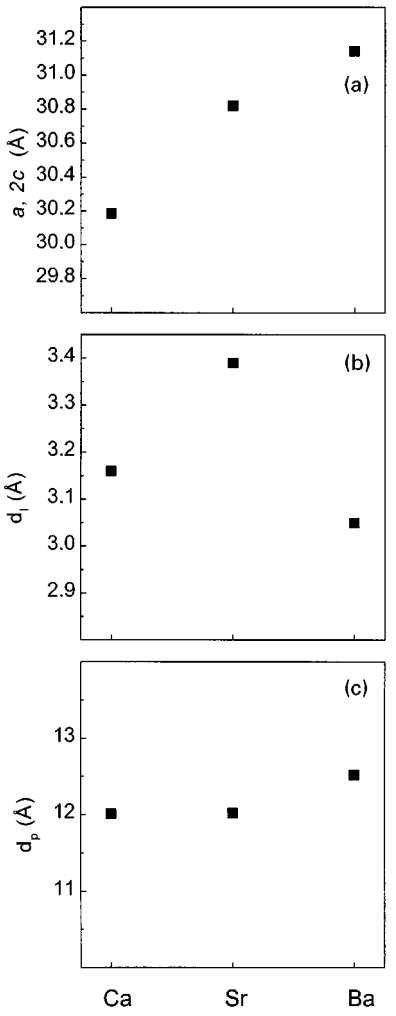

FIG. 7. (a) Lattice parameter (a, $2c$) perpendicular to the perovskite slab, (b) thickness of the Cs^+ interlayer space (in between the two triple-perovskite slabs), and (c) thickness of triple-perovskite slab $[A_2Nb_3O_{10}]^-$ in layered perovskites of the series $CsA_2Nb_3O_{10}$ (A = Ca, Sr and Ba).

than in the case of Sr– or Ba–O bonds. Therefore, one would expect that the Ca compounds would exhibit higher ionic conduction. This may be an another explanation for the higher conductivity of the $CsCa_2Nb_3O_{10}$ compared to Sr and Ba compounds. A similar effect has been realized in the case of our recent investigations on Li-ion conductivity based on the 3D perovskites (Li, La)TiO_3 where substitution of 0.05 mol% Al at the B–(Ti) site increases the Li-ion conductivity as compared to that of undoped material (23).

3.4.2. Electrical conductivity of $CsSr_2Ta_3O_{10}$. The conductivity of the Ta compound, $CsSr_2Ta_3O_{10}$, is different from that of the corresponding Nb compound. There is a break in the conductivity value at around 700°C during the first heating cycle (Fig. 12). Data obtained during the second cooling cycle and third heating and cooling cycle follow the same line with an activation energy of 0.78 eV. A similar break in the conductivity value is obtained at 330°C for $AgLaNb_2O_7$ (5) ($n = 2$ member of D-J series) and at about 520°C for $Na_2La_2Ti_3O_{10}$ ($n = 3$ member of the R-P series) layered perovskites. The break in the conductivity of the first compound is due to the structural phase transition from the low-temperature phase (tetragonal phase with phase group $I4_1/acd$) to the high-temperature phase (tetragonal phase with space group $I4/mmm$). The main structure difference between the two phases is due to the arrangement of interlayer Ag ions. In the case of the latter compound, the break in the conductivity may be due to the structural disorder; the exact reason is presently not known. However, a similar conductivity behavior (break in the Arrhenius plot) has not been observed for other isostructural layered perovskite members of the same family, viz., $ALaNb_2O_7$ (A = Li, Na, K) and $A_2Nd_2Ti_3O_{10}$ (A = K) (5).

In order to understand the break in the conductivity value of $CsSr_2Ta_3O_{10}$ at 700°C, we performed DTA measurements (2°C/min) up to 850°C for two subsequent heating and cooling cycles in air with different amounts of the samples (80 and 330 mg). We did not observe any exothermic peak up to 850°C in the DTA and no weight loss in the TGA. Powder XRD data of $CsSr_2Ta_3O_{10}$ remain the same both before and after TGA–DTA measurements. The decrease in the conductivity may be due to disorder in the interlayer alkali ions or phase change, or the activity of the alkali metal may change by the formation of a thin layer of the reaction products at the surface of the pellet at elevated temperature. Further clarification is necessary.

3.4.3. DC measurements. In order to obtain direct information on the type of charge carriers, DC measurements

TABLE 3
Selected Bond Lengths (Å) for $A'[A_2B_3O_{10}]$
(A' = Rb, Cs; A = Ca[a], Sr, Ba; B = Nb, Ta)

	Compound			
Bond	$RbSr_2Nb_3O_{10}$	$CsSr_2Nb_3O_{10}$	$CsBa_2Nb_3O_{10}$	$CsSr_2Ta_3O_{10}$
A′–O4	8 × 3.15(2)	8 × 3.24(3)	8 × 3.20(2)	8 × 3.19(2)
A–O3	4 × 2.66(2)	4 × 2.62(3)	4 × 2.77(2)	4 × 2.62(2)
A–O2	4 × 2.77(1)	4 × 2.78(1)	4 × 2.83(1)	4 × 2.77(1)
A–O1	4 × 2.96(1)	4 × 2.96(1)	4 × 2.99(1)	4 × 2.97(1)
B1–O1	4 × 1.95(1)	4 × 1.95(1)	2 × 1.89(3)	4 × 1.95(1)
B1–O2	2 × 1.96(3)	2 × 1.97(5)	4 × 1.99(1)	2 × 1.98(2)
B2–O4	1.71(4)	1.65(6)	1.74(3)	1.76(3)
B2–O3	4 × 1.98(1)	4 × 1.20(1)	4 × 2.02(1)	4 × 1.99(1)
B2–O2	2.44(3)	1 × 2.41(5)	2.64(3)	2.42(2)

[a]Cs–O bond lengths in $CsCa_2Nb_3O_{10}$: Cs(1)–O2 (2 × 3.08 Å, 2 × 3.29 Å); Cs(1)–O3 (2 × 3.10 Å, 2 × 3.23 Å); Cs(2)–O2 (2 × 3.16 Å, 2 × 3.21 Å); Cs(2)–O3 (2 × 3.02 Å, 2 × 3.28 Å) (Ref. 20).

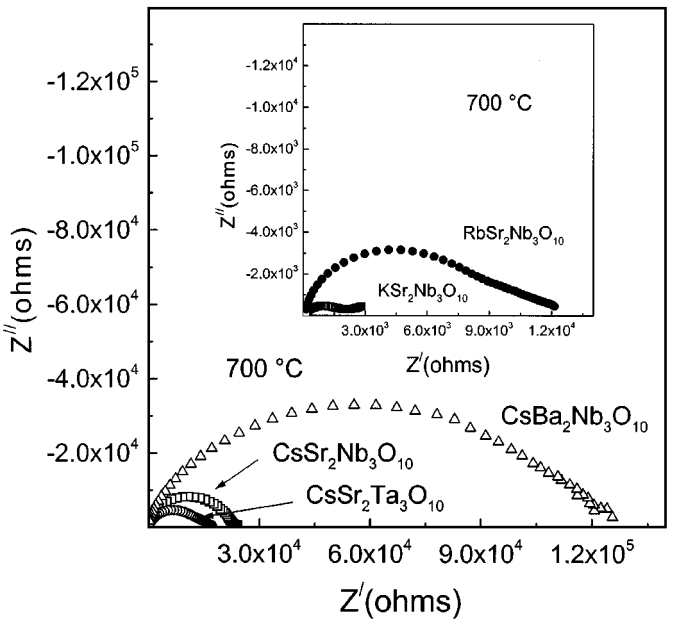

FIG. 9. Typical impedance plots for $KSr_2Nb_3O_{10}$, $RbSr_2Nb_3O_{10}$, $CsSr_2Nb_3O_{10}$, $CsBa_2Nb_3O_{10}$, and $CsSr_2Ta_3O_{10}$ obtained in air at 700°C.

were performed. Inert and ionically blocking platinum electrodes were applied for a voltage range from 0 to 0.6 V. The steady state current response is shown in Fig. 13 in the case of $RbSr_2Nb_3O_{10}$ in air at 620°C. Only electronic charge carriers may be transferred in steady state in this type of experiment. The linear representation of the current vs voltage shows a conductivity of the sample of $2–7 \times 10^{-6}$ S/cm when the data are interpreted by assuming Ohm's law. This value corresponds roughly to the result obtained by impedance measurements which gives an interpolated value of 1×10^{-5} S/cm. The logarithmic representation of the current vs voltage (Fig. 13, inset) indicates a slope of 2.5 V^{-1}. Assuming a transfer of electrons by diffusion, as in the case of a Hebb–Wagner polarization (24) measurement, a slope of 5.64 V^{-1} would be expected when a reversible reference electrode is used at one side. The latter is not the case in the

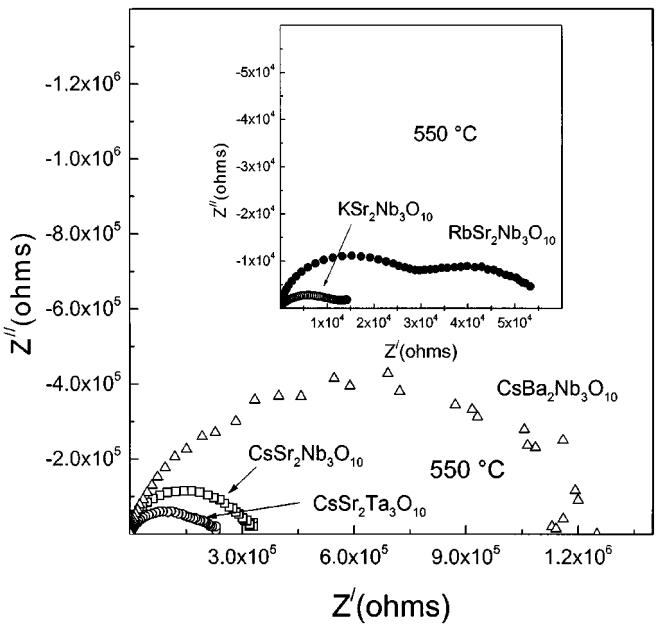

FIG. 8. Typical impedance plots for $KSr_2Nb_3O_{10}$, $RbSr_2Nb_3O_{10}$, $CsSr_2Nb_3O_{10}$, $CsBa_2Nb_3O_{10}$ and $CsSr_2Ta_3O_{10}$ obtained in air at 550°C.

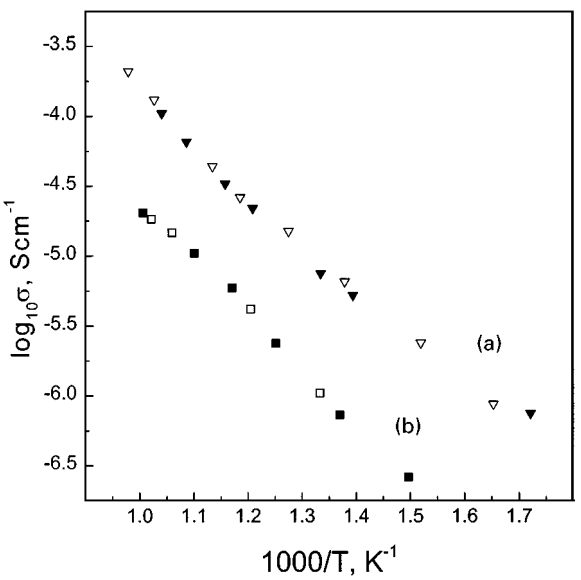

FIG. 10. Arrhenius plots of the total electrical conductivity of (a) $KSr_2Nb_3O_{10}$ and (b) $RbSr_2Nb_3O_{10}$. Open and closed data points represent the heating and cooling cycles.

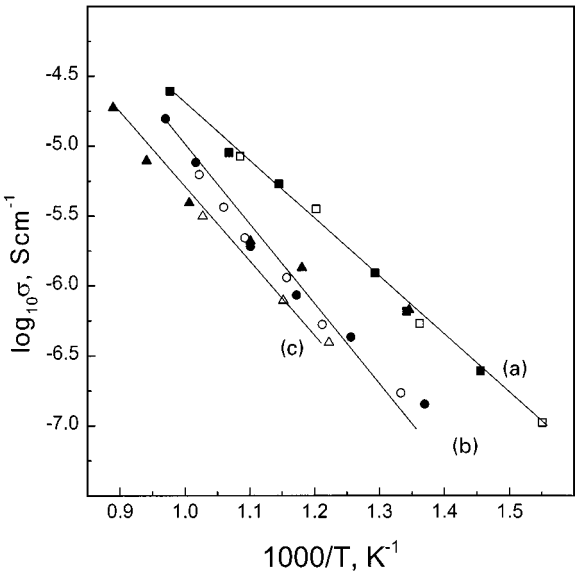

FIG. 11. Arrhenius plots of the total electrical conductivity of (a) $CsCa_2Nb_3O_{10}$, (b) $CsSr_2Nb_3O_{10}$, and (c) $CsBa_2Nb_3O_{10}$. Open and closed data points represent the heating and cooling cycles. The lines connecting the data points are guides to the eye.

present experiment and a smaller slope may be well expected since both concentrations of electronic charge carriers change at the two electrodes by the applied voltage.

The change in the slope in the linear current vs voltage representation (Fig. 13) indicates the presence of ionic

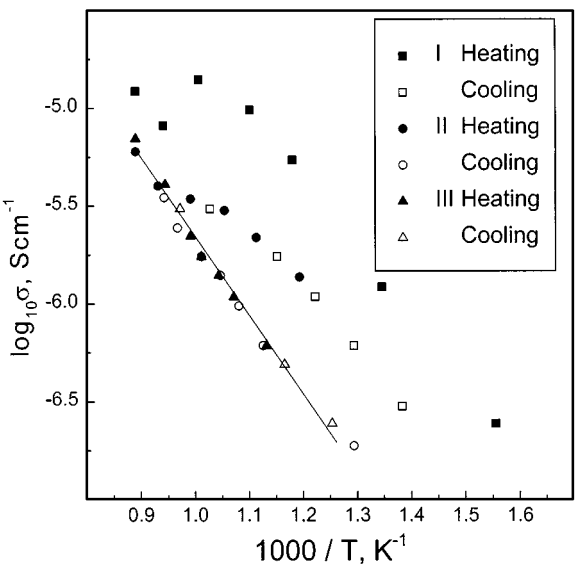

FIG. 12. Arrhenius plots of the total electrical conductivity of $CsSr_2Ta_3O_{10}$. The lines connecting the data points are guides to the eye. We see a break in the electrical conductivity data at around 700°C in the first heating cycle. Data from the second cooling and third heating and cooling cycles fall on the same line. The lines connecting the data points are guides to the eye.

TABLE 4
Electrical Conductivity Data of $A'[A_2B_3O_{10}]$
(A' = K, Rb, Cs; A = Ca, Sr, Ba; B = Nb, Ta)

Compound	$\sigma_{700°C}$ (S/cm)	E_a (eV)
$KSr_2Nb_3O_{10}$	1.46×10^{-4}	0.70 (330–570°C)
$RbSr_2Nb_3O_{10}$	1.78×10^{-5}	0.79 (400–725°C)
$CsCa_2Nb_3O_{10}$	1.45×10^{-5}	0.83 (370–750°C)
$CsSr_2Nb_3O_{10}$	6.01×10^{-6}	1.00 (460–750°C)
$CsBa_2Nb_3O_{10}$	3.45×10^{-6}	0.92 (550–840°C)
$CsSr_2Ta_3O_{10}$	1.78×10^{-6}	0.78 (500–850°C)

charge transfer. This is supported by the time dependence of the current after a fixed voltage is applied. This is shown in Fig. 14 for the example of the application of 0.3 V to the same $RbSr_2Nb_3O_{10}$ sample at the same temperature of 620°C. A fast response would be expected in the case of a predominant electronic conductor without ionic motion. The time dependence of the response may be interpreted only by the motion of ions that are assumably alkaline ions. The applied electrical voltage generates different Fermi levels of the electrons at both interfaces with the electrodes. As a result, ions are moving toward the interface with an increase in the alkali metal concentration at the negative electrode and a decrease at the positive electrode. By the local variation of the composition, the electronic charge carrier concentration changes locally and accordingly the integral of the resistance over the sample is changed and causes the time dependence. The process is controlled by

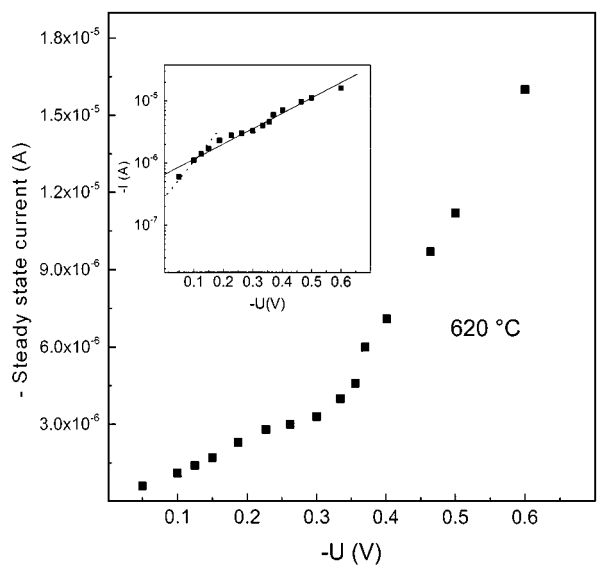

FIG. 13. Steady-state electrical current (I) as a function of applied voltage (V) at 620°C for $RbSr_2Nb_3O_{10}$ in air. (Inset) Log I as a function of applied voltage.

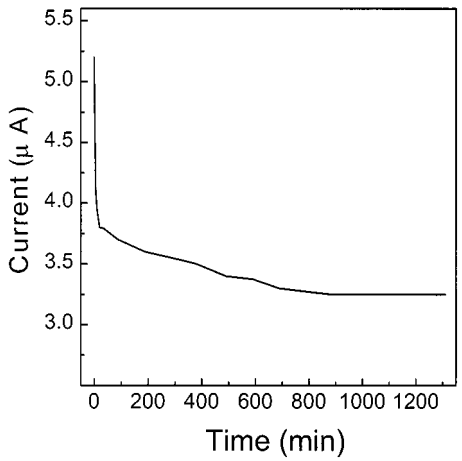

FIG. 14. Time dependence of the electrical current (I) at fixed voltage of 0.3 V for $RbSr_2Nb_3O_{10}$ in air.

a chemical diffusion process, i.e., by the influence of an electrochemical potential gradient. The diffusion coefficient for the motion of ions may be approximated by the equation for the mean square displacement ($\tau = L^2/D$), where τ is the equilibration time, L the thickness of the sample, and D the diffusivity. Assuming an equilibration time of 800 minutes and assuming that the chemical diffusion coefficient is of the same order of magnitude as the diffusivity, the conductivity for the rate determining charge carriers is approximately 6×10^{-4} S/cm, when the concentration of alkaline ions is taken as 4.32×10^{21} cm^{-3} according to the structure of the material. This value is more than one order of magnitude larger than the conductivity obtained from impedance measurements. Assuming the Hebb–Wagner polarization, the electronic conductivity would be about 10^{-6} S/cm from taking into account the intersection of the straight line with the log I axis (Fig. 13).

In view of the polarization measurements and blocking of the ionic charge carriers, it is clearly observed that layered perovskites exhibit both ionic and electronic conduction. Further experimental arrangements with different types of electrodes will be necessary to obtain more information on the transport of alkali ion in these materials.

4. CONCLUSION

The divalent alkaline earth ion (Ca^{2+}) in the D-J series $A'Ca_2B_3O_{10}$ ($A' = $ K, Rb, Cs; $B = $ Nb, Ta) has been replaced by other alkaline earth ions by solid-state reactions. Both the Sr- and the Ba-containing compounds are isostructural with the corresponding Ca compounds. The lattice parameters increase as the size of the alkaline ion size increases in the series. Among the investigated series $CsA_2B_3O_{10}$ ($A = $ Ca, Sr, Ba), $CsCa_2Nb_3O_{10}$ exhibits the highest conductivity of 1.45×10^{-5} S/cm at 700°C with an activation energy of 0.83 eV which is comparable to the values reported in the literature. The low electrical conductivity of Sr and Ba compounds may be due to shorter Cs–O bonds than in Ca compound. DC measurements reveal that the layered perovskites exhibits both ionic and electronic conduction. However, the conductivity could be predominantly ionic in nature.

ACKNOWLEDGMENTS

The authors thank Professor R. A. Huggins for useful discussions and Mr. Thomas Metzing for technical support.

REFERENCES

1. M. Dion, M. Ganne, and M. Tournoux, *Mater. Res. Bull.* **16,** 1429 (1981); A. J. Jacobson, J. T. Lewandowski, and J. W. Johnson, *J. Less-Common Met.* **116,** 137 (1986); J. Gopalakrishnan, V. Bhat, and B. Raveau, *Mater. Res. Bull.* **22,** 413 (1987).
2. S. N. Ruddlesden and P. Popper, *Acta Crystallogr.* **10,** 538 (1957); S. N. Ruddlesden and P. Popper, *Acta Crystallogr.* **11,** 54 (1958).
3. J. Gopalakrishnan and V. Bhat, *Inorg. Chem.* **26,** 4299 (1987).
4. A. J. Jacobson, J. W. Johnson, and J. T. Lewandowski, *Inorg. Chem.* **24,** 3727 (1985); K. A. Hyeon and S. H. Byeon, *Chem. Mater.* **11,** 352 (1999).
5. M. Sato, J. Abo, T. Jin, and M. Ohta, *J. Alloys Compd.* **192,** 81 (1993); M. Sato, J. Watanabe, and K. Uematsu, *J. Solid State Chem.* **107,** 460 (1993); R. Marchand, L. Brohan, and M. Tournoux, *J. Solid State Chem.* **112,** 345 (1994); K. Toda, Y. Kameo, S. Kurita, and M. Sato, *J. Alloys Compd.* **234,** 19 (1996); S. H. Byeon and K. Park, *J. Solid State Chem.* **121,** 430 (1996).
6. M. Fang, C. H. Kim, and T. E. Mallouk, *Chem. Mater.* **11,** 1519 (1999).
7. H. Fukuoka, T. Isami, and S. Yamanaka, *Chem. Lett.* **8,** 703 (1997); Y. Takano, S. Takayanagi, S. Ogawa, T. Yamadaya, and N. Mori, *Solid State Commun.* **103,** 215 (1997).
8. G. Blasse and A. Bril, *J. Chem. Phys.* **48,** 3652 (1968); K. Toda, Y. Kameo, M. Ohta, and M. Sato, *J. Alloys Compd.* **218,** 228 (1995); A. Kudo and T. Sakata, *J. Phys. Chem.* **99,** 15963 (1995); A. Kodo, *Chem. Mater.* **9,** 664 (1997).
9. K. Domen, J. Yoshimura, T. Sekine, A. Tanaka, and T. Onishi, *Catal. Lett.* **4,** 339 (1990); J. Yoshimura, Y. Ebina, J. N. Kondo, K. Domen, and A. Tanaka, *J. Phys. Chem.* **97,** 1970 (1993); Y. Ebina, A. Tanaka, J. N. Kondo, and K. Domen, *Chem. Mater.* **8,** 2534 (1996); S. Ikeda, A. Tanaka, M. Hara, J. N. Kondo, K. Maruya, and K. Domen, *Microporous Mater.* **9,** 253 (1997); S. Ikeda, M. Hara, J. N. Kondo, K. Domen, H. Takahashi, T. Okubo, and M. Kakihana, *Chem. Mater.* **10,** 72 (1998).
10. Y. Moritomo, A. Asamitsu, H. Kuwahara, and Y. Tokura, *Nature* **380,** 141 (1996); M. Suzuki, F. Kanamaru, K. Toda, and T. Sakai, *in* "Electroceramics in Japan II, CSJ Series," (N. Mitzutani, K. Shinozaki, N. Kamehara, and T. Kimura, Eds.), Vol. 5, p. 239, Trans. Tech. Publications; Y. Breard, C. Michel, M. Hervieu, and B. Raveau, *J. Mater. Chem.* **10,** 1043 (2000).
11. R. Seshadri, C. Martin, M. Herien, B. Raveau, and C. N. R. Rao, *Chem. Mater.* **9,** 270 (1997); P. D. Battle, M. A. Green, N. S. Laskey, J. E. Millburn, L. Murphy, M. J. Rosseinsky, S. P. Sullivan, and J. F. Vente, *Chem. Mater.* **9,** 552 (1997).
12. J. Gopalakrishann, *Chem. Mater.* **7,** 1265 (1995).
13. M. A. Subaramanian, J. Gopalakrishnan, and A. W. Sleight, *Mater. Res. Bull.* **23,** 837 (1988); S. Uma, A. R. Raju, and J. Gopalakrishnan, *J. Mater. Chem.* **3,** 709 (1993).

14. N. S. P. Bhuvanesh, M. P. Crosnier-Lopez, and J. L. Fourquet, *J. Mater. Chem.* **9,** 3093 (1999); N. S. P. Bhuvanesh, M. P. Crosnier-Lopez, O. Bohnke, J. Emery, and J. L. Fourquet, *Chem. Mater.* **11,** 634 (1999); N. S. P. Bhuvanesh, M. P. Crosnier-Lopez, H. Duroy, and J. L. Fourquet, *J. Mater. Chem.* **10,** 1685 (2000).
15. S. H. Byeon and H. J. Nam, *Chem. Mater.* **12,** 1771 (2000).
16. C. L. Lengauer, HILL, Institut für Mineralogie, Kristallographie und Strukturchemie der Universität Wien, 1993.
17. J. Rodrigues-Carvajal, FULLPROF, version 3. Abstracts of the Satellite Meeting on Powder Diffraction of the Fifteenth Congress of the International Union of Crystallography, Toulouse, 1990.
18. K. Toda, T. Teranishi, Z. G. Ye, M. Sato, and Y. Hinatsu, *Mater. Res. Bull.* **34,** 971 (1999).
19. M. Dion, M. Ganne, and M. Tournoux, *Rev. Chim. Miner.* **23,** 61 (1986); H. Fukuoka, T. Isami, and S. Yamanaka, *J. Solid State Chem.* **151,** 40 (2000).
20. M. Dion, M. Ganne, and M. Tournoux, *Rev. Chim. Miner.* **21,** 92 (1984).
21. R. D. Shannon, *Acta Crystallogr. A* **32,** 751 (1976).
22. I. Barin, "Thermodynamic Data of Pure Substances," Part 1 and 2. VCH, New York, 1993.
23. V. Thangadurai and W. Weppner, *Ionics* **6,** 70 (2000).
24. M. H. Hebb, *J. Chem. Phys.* **20,** 185 (1952); C. Wagner, "Proceedings, 7th Meeting of the International Committee of Electrochemical Thermodynamics and Kinetics, (CITCE), Lindau," pp. 361–377 Butterworths, London, 1957.